Research Article

Mario Versaci*, Giovanni Angiulli, Paolo di Barba, and Francesco Carlo Morabito

Joint use of eddy current imaging and fuzzy similarities to assess the integrity of steel plates

https://doi.org/10.1515/phys-2020-0159
received January 3, 2020; accepted May 18, 2020

Abstract: Steel plates bi-axially loaded are characterized by mechanical deformations whose 2D image representations are very difficult to achieve. In this work, the authors propose an innovative approach based on eddy current techniques for obtaining 2D electrical maps to assess the mechanical integrity of a steel plate. The procedure, also exploiting fuzzy similarity computations, translates the problem of the assessment of the mechanical integrity of a steel plate into a suitable classification problem. The results obtained by this proposed procedure show performances comparable to those provided by well-established soft computing approaches with a higher computational complexity.

Keywords: non-destructive testing and evaluation, eddy currents, soft computing, fuzzy similarities, classification problems

1 Introduction to the problem

Metal structures represent one of the greatest achievements of civil engineering as it is a combination of high mechanical properties with a significant reduction in the mass of buildings compared to other construction techniques, such as reinforced concrete, in which the mass is significant.[1] However, in steel buildings, there are structural elements, such as connecting plates, which are more stressed than others and subject to compound external loads such as the bi-axial traction [1]. Hence, there is a need to periodically evaluate the state of health of these plates by non-destructive testing and evaluation (NDT/NDE) to quantify the distribution of the deformations [2–4] as they could produce excessive internal mechanical tensions [1]. Ferrous materials, such as steels, often highlight inhomogeneities that lead to a phenomenon of electrical run outs that cause unwanted phenomena of uncertainty in the measurements. This could arise from the numerous heat treatments during the manufacture of the product which alter the microstructures causing strong changes in the properties of the material [5]. Furthermore, the metallurgy of the material itself can lead to the modification of the crystal lattice, which leads to the random variation in both magnetic permeability and electrical conductivity [5]. In [6,7], such phenomenon has been studied in the case of finite elasticity, modeling the microstructure in terms of bi-phase materials (derived from the solid-to-solid transformations) and achieving the distribution of deformations as a function of the external bi-axial load applied [8]. Although theoretically interesting and potentially applicable in different fields (necking, shear-band, etc.), this model [6] presents difficulties in obtaining deformations, except for simple geometries and constant boundary conditions along the edges of the plates [1]. Accordingly, the numerical approach results to be the most appropriate to tackle this problem, but the reduced possibility of obtaining analytical existence/uniqueness conditions for this model does not prevent it from being affected by possible ghost solutions [9]. Anyway, the model [6] is theoretically able to produce 2D maps of the amplitude of the mechanical deformation, so that, through

* **Corresponding author: Mario Versaci,** DICEAM Department, Mediterranea University, Reggio Calabria, Italy, e-mail: mario.versaci@unirc.it
Giovanni Angiulli: DIIES Department, Mediterranea University, Reggio Calabria, Italy, e-mail: giovanni.angiulli@unirc.it
Paolo di Barba: Department of Electrical Computer and Biomedical Engineering, University of Pavia, Italy, e-mail: paolo.dibarba@unipv.i
Francesco Carlo Morabito: DICEAM Department, Mediterranea University, Reggio Calabria, Italy, e-mail: morabito@unirc.it

1 Seismic actions on a building are proportional to the mass of the building itself, whereby high masses involve higher seismic stresses.

the constitutive laws, it is possible to find the 2D maps of internal mechanical stresses [1,10], useful to evaluate the state of health of the plate. Unfortunately, these maps[2] require a high computational load for being computed, which makes them useless for real-time applications. In addition, in the framework of small deformations, the evaluation of the plate deformations may not provide useful results, due to the very low values of their amplitudes. Then, it is preferred to know the external bi-axial load producing the detected deformation state to understand if the steel plate has been overstressed. This way (i.e., starting from the distribution of the deformations to achieve the external bi-axial load), we make this inverse problem into a classification one. With these premises, the idea we propose in the present work exploits the fact that, from an experimental point of view, the 2D maps of the mechanical deformations obtainable under the same external bi-axial load conditions [6,7] are equivalent to those obtained by inducing eddy currents (ECs) in the plate and measured by a FLUXSET-type probe [3,11,12] moved by an automatic step-by-step device along x and y axes with the aim to pick-up the voltage (Figure 1) [13]. On the sidelines, let us propose a further figure (Figure 2) extracted from the center of 2D ECs of Figure 1, which shows a kind of opening in its central zone. Since similar bi-axial loads (which are close to each other in terms of amplitudes) applied to a plate produce similar deformations on it [1,10], they can be grouped into a single class of loads. Furthermore, for each applied load similar to a predetermined load k, the related EC map can be evaluated to obtain a "class" of similar images. If the preset bi-axial loads are $\tilde{N}$, then $\tilde{N}$ classes of bi-axial loads are considered (Class 1, Class 2,...,Class k,..., Class $\tilde{N}$). Also, an additional class, obtained from the 2D maps of plates not subjected to any load (Figure 3), is considered. From the set of 2D maps belonging to each class, we obtain a single 2D map representing each class by using fuzzy image fusion techniques. At this point, the 2D EC map obtained by applying on plate under test an unknown external bi-axial load is compared to the representative images of the $\tilde{N} + 1$ classes using algebraic techniques of similarity, hence obtaining $\tilde{N} + 1$ similarity values. The higher similarity value determines the membership of the unknown map at hand to the bi-axial load class that generated the maximum similarity value. However, due to the nature of the EC maps, the transitions between the different zones in the images appear not clearly defined (i.e., characterized by low gradients of gray level values). From which, the need to reformulate the problem of the similarity computation in fuzzy terms [14,15] by exploiting specific fuzzy similarity (FS) indexes [16–20]. The remainder of the article is structured as follows: Section 2 explains the theoretical principles of the Chao–Chen model [6,7], while Section 3 details the database developed at the Electrotechnics – NDT/NDE

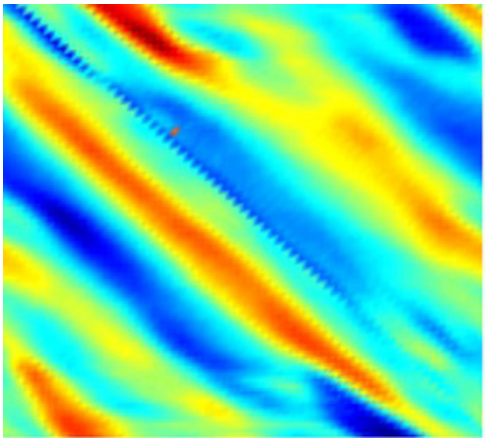

Figure 1: A typical 2D EC map when an external bi-axial load is applied.

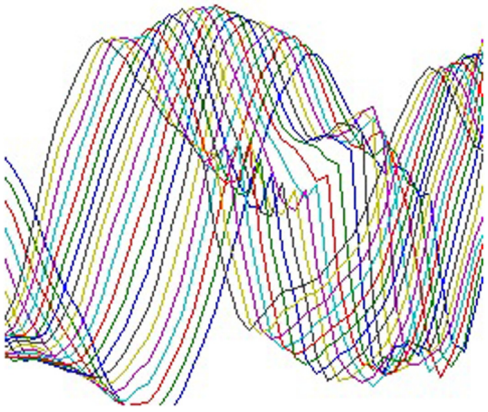

Figure 2: Central area of the 2D EC map depicted in Figure 1.

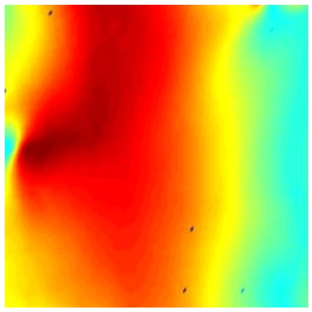

Figure 3: 2D EC map when no external bi-axial load is applied.

2 There is no experimental instrumentation able to derive such deformations so that it is necessary to get them analytically.

Table 1: List of the acronyms

Acronym	Description	Acronym	Description
NDT/NDE	Non-destructive testing and evaluation	EC	Eddy current
AC	Alternative current	RMS	Root mean square
IoF	Index of fuzziness	AFD	Axiomatic fuzzy divergence
FIS	Fuzzy inference system	FKM	Fuzzy *K*-means
SOM	Self-organizing map	I/O	Input/output

Laboratory of the "Mediterranea" University of Reggio Calabria. Sections 4–6 describe in-depth the proposed approach motivating the operational choices made and the approaches exploited to compare the obtained results, respectively. Numerical results are presented and discussed in Section 7. Finally, in Section 8, some conclusions are drawn. To increase the readability of the text, Tables 1 and 2 list the acronyms and symbols exploited, respectively.

2 Some theoretical backgrounds

According to Chen's theory, it is known that energy plays a key role to study problems concerning the stress–deformation relationship [6]. With this premise, let us introduce the following definitions.

Definition 1. (Set of 2D isochoric deformations) Let us indicate by Ω a homogeneous, regular and bounded region of $\mathbb{R}^2$, whose boundary is $\partial\Omega$, occupied by an elastic body composed of a homogeneous, incompressible and isotropic material. If an external bi-axial load is applied on Ω, an isochoric deformation $\vec{d}$ [3] such that $\vec{d} \in C^1(\bar{\Omega}, \mathbb{R}^2)$ is produced. Then, let us indicate by M the class of isochoric deformations, i.e., the class of deformations such that $\nabla\vec{d} = \underline{\underline{H}}$ with $|\underline{\underline{H}}| = 1$ [6]:

$$\vec{d} \in M = \{\vec{d} \in C^1(\bar{\Omega}, \mathbb{R}^2): \underline{\underline{H}} = \nabla\vec{d}, |\underline{\underline{H}}| = 1\}, \quad (1)$$

where $\underline{\underline{H}}$, being a gradient of a vector, is a second-order tensor (i.e., a matrix). Moreover, $\underline{\underline{H}}^{-1} = \underline{\underline{H}}^T$ so that $\underline{\underline{H}}$ is an orthogonal matrix [6].

Definition 2. (The principal stretches) Once $\underline{\underline{H}}$ has been defined (see Definition 1), let us consider the following stretch tensor:

$$\sqrt{\underline{\underline{H}}\ \underline{\underline{H}}^T}, \quad (2)$$

where $\underline{\underline{H}}\ \underline{\underline{H}}^T$ represents the left Cauchy–Green's tensor. The eigenvalues of (2), λ_1 and λ_2, represent the principal stretches of the deformation [6].

2.1 Stored energy

Indicating by Y the strain-energy function of the material, it can be expressed in the following form [6]:

Table 2: List of the exploited symbols

Symbol	Description	Symbol	Description
$\tilde{N}$	Number of preset bi-axial loads	$\vec{d}$	Isochoric deformation
M	Class in which d is defined	$\underline{\underline{H}} = \nabla\vec{d}$	Deformation gradient
$Y(\lambda_1, \lambda_2)$	Stored energy	λ_1, λ_2	Eigenvalues of the stretch tensor
Ω	Homogeneous, regular and bounded body	$\partial\Omega$	Boundary of Ω
$\vec{t}$	Traction vector	$\underline{\underline{I}}$	Constant traction tensor
$\hat{n}$	Outward normal on $\partial\Omega$	$\underline{\underline{S}}(\underline{\underline{H}}^+)$	Kirchhoff–Piola tensor
I	EC map	a_{ij}	Gray levels of I
$m_I(a_{ij})$	Fuzzy membership function	$F(I)$	Fuzzified image
F_e, F_d	Fuzzifiers	$\widehat{m_I(a_{ij})}$	Nearest ordinary set
$F(\mathbf{I_x})$, $F(\mathbf{I_y})$	Generic $F(\mathbf{I})$	U	Universe of discourse
$F(\mathbf{I_{un}})$	$F(\mathbf{I})$ for an unknown load	$F(\mathbf{I}_{\text{No Load}})$	$F(\mathbf{I})$ without loads
$F(\mathbf{I_k}^s)$, $F(\mathbf{I_k}^z)$	Two generic images in the class $\mathbf{k}$		

$$Y = Y(\lambda_1, \lambda_2), \tag{3}$$

where, in particular, $Y \in C^{\infty}(\Omega)$. If the body is subjected to a dead-load surface traction (e.g., when a bi-axial load is applied), it makes sense to write:

$$\vec{t} = \underline{\underline{T}} \cdot \hat{n} \text{ on } \partial\Omega, \tag{4}$$

where $\underline{\underline{T}}$ is a constant traction tensor, $\hat{n}$ is the unit outer normal to $\partial\Omega$ and $\vec{t}$ is the traction vector (obviously, measured in the reference configuration). Then, exploiting the well-known energy stability criterion, a deformation $\vec{d}$ can be considered as stable if it is a weak minimizer of the following total energy G [6]:[4]

$$G = \int_{\Omega} [Y(\lambda_1, \lambda_2) - \underline{\underline{T}} \cdot \nabla \vec{d}] \, d\Omega, \tag{5}$$

where G is defined on M and admits a minimum value if and only if the equilibrium conditions occur [6].

Remark 1. This model describes in detail both equilibrium states and stability. However, it is worth noting that it neglects all the microstructural effects.

Remark 2. In the framework of finite elasticity, a lot of materials support fields characterized by strong gradient of discontinuity where smooth variation in deformations takes place except for particular sections on which the gradient gap can occur.

Remark 3. In the framework of plastic deformations, shear-band formations in Ω can occur compromising the integrity of the material constituting Ω.

2.2 Minimization problem

As known, $\underline{\underline{H}}$ represents a local minimum for each point of discontinuity. Then, indicating by $\underline{\underline{H}}^+$, $\underline{\underline{H}}^-$ the gap of $\underline{\underline{H}}$ on a point of discontinuity, the deformation $\vec{d}$ corresponding to $\underline{\underline{H}}^+$, $\underline{\underline{H}}^-$ is a global minimum. Then, taking into account that Y depends on $\underline{\underline{H}}$, the following equality yields:

$$Y(\underline{\underline{H}}^+) - Y(\underline{\underline{H}}^-) = \underline{\underline{S}}(\underline{\underline{H}}^{\pm}) \cdot (\underline{\underline{H}}^+ - \underline{\underline{H}}^-), \tag{6}$$

where $\underline{\underline{S}}(\underline{\underline{H}}^{\pm})$ represents the Piola–Kirchhoff tensor. As required by Hadamard's theory, conditions of geometric compatibility satisfying across an interface separating regions deformed with gradient $\underline{\underline{H}}^+$, $\underline{\underline{H}}^-$ are assumed that there are vectors $\vec{a} \in \mathbb{R}^2$ and $\vec{n} \in \mathbb{R}^2$ in order that

$$\underline{\underline{H}}^+ - \underline{\underline{H}}^- = \vec{a} \otimes \vec{n}. \tag{7}$$

Therefore, it is possible to build a continuous piecewise affine deformation $\vec{d}$ through a set of layers characterized by deformation gradients $\underline{\underline{H}}^+/\underline{\underline{H}}^-/\underline{\underline{H}}^+/\underline{\underline{H}}^-, \ldots$ In [21,22], it has been proved that it is possible to arrange a fine mixture of the layers $\underline{\underline{H}}^+/\underline{\underline{H}}^-/\underline{\underline{H}}^+/\underline{\underline{H}}^-, \ldots,$ on a side of an appropriately oriented interface in order that the average deformation gradient of these layers satisfies the conditions of compatibility. These configurations can be interpreted from an energetic point of view. In particular, they represent a minimizing sequence rather than minimizers. In other words, each of the minimizing sequences weakly converges to a deformation $\vec{d}^{\star}$ that is not a minimizer of the total free energy. Then, Y is not lower semicontinuous with respect to the weak convergence in $W^{1,p}(\Omega, \mathbb{R}^2)$, with $p \geq 1$. It is worth noting the fact that the lower semicontinuity fail is a typical property of free energy-based functionals for phase changing solids. This is caused by the non-ellipticity of these functional ones. Furthermore, by comparing the theory with experimentation, the detailed structure of the minimizing sequences is as important as the minimizers. In fact, it is well known that, in the absence of ellipticity conditions, the integrals of the calculation of the variations do not reach a minimum between the ordinary functions, but reach a minimum in a space of "generalized curves", which represent the limits of minimizing sequences that fluctuate more and more finely [21]. It was demonstrated (for details see [21]) that in the 2D case the deformation $\vec{d}^{\star}$ admits global stability if and only if

$$Y(\vec{d}^{\star}) \leq Y(\vec{d}). \tag{8}$$

In other words, $\vec{d}^{\star}$ is a minimizer for Y in the deformation admissible set.

Although this approach is theoretically interesting for recovering d, it involves a high computational burden, making it unsuitable for real-time applications.

Then, we here propose a new fuzzy procedure with low computational complexity that, exploiting the 2D EC maps [3,18], associates an unknown deformation distribution[5] to an external bi-axial load.

---

3 An isochoric deformation is a first-order tensor, i.e., a vector.

4 $\underline{\underline{T}} \cdot \nabla \vec{d}$ is a scalar because it is a saturation product.

5 The EC distributions in a plate are closely linked to the plate's deformation d.

3 Experimental database

3.1 Experimental campaign of measurements

It was developed at the "Mediterranea" University of Reggio Calabria (Italy) – Laboratory of Electrotechnics and NDT/NDE. A set of 180 mm × 180 mm × 5 mm S 235 steel plates for civil buildings[6] were subjected to symmetrical and gradually increasing bi-axial loads and, then, investigated. For the training step, the plate was subjected to the load starting from 160 kN to the final load of 200 kN, with steps of 10 kN. Because of the microscopic structure of the material, each external load modifies locally the magnetic properties of the plate. Accordingly, its state of degradation was investigated by analyzing the magnetic changes induced in the structure of the material when the deformations take place. The probe [3] consists of three coils: (1) an exciting coil to induce EC in the specimen (outer diameter = 10 mm, inner diameter = 6 mm and length = 5 mm) and a FLUXSET® sensor (length = 6 mm and diameter = 1.2 mm) which is located between the exciting coil and the plate; (2) a driving coil; and (3) a pick-up coil. Moreover, the approximate lift-offs for both the exciting coil and the sensor are 2 and 0.6 mm, respectively. The pick-up voltage provides a measure, which is proportional to the component of the amplitude of the magnetic field, $|\mathbf{H}|$, parallel to the longitudinal axis of the sensor. In addition, both an AC sinusoidal exciting field (1 kHz) and an electric current (120 mA RMS) have been applied. With regard to the driving signal, the choice fell on a triangular shape at the frequency of 100 kHz with 2 V_{pp} amplitude.

3.2 EC imaging

The sensor was assembled to a 0.5 mm step-by-step automatic scanning system moved on a square portion (70 mm side) at the middle of the specimen to map the area where maximum deformation is more likely to occur (e.g., see Figure 2). After each symmetrical bi-axial load application, the specimen was investigated by means of the probe obtaining four 2D signal representatives of the real part, the imaginary part, the module and the phase of the pick-up voltage (mV) at each point of the surface of the specimen. Each 2D signal achieved represents a matrix that, by means of MatLab Toolbox®, has been transformed into a 2D image in which each pixel represents a single measurement sampled by the probe in a specific position of the step-by-step scanning system (e.g., see Figure 1). Therefore, the achieved 2D image[7] is significant of the distribution of the deformations on the specimen. For each specimen, four 2D images were obtained related to the real part, imaginary part, module and phase of the pick-up voltage, respectively. Since similar loads provide similar deformations (characterized by similar magnetic properties), a series of gradually increasing bi-axial loads were applied to the plate, obtaining in this way five classes of images (60 × 4 images for each class): $C_{160\ kN}$, $C_{170\ kN}$, $C_{180\ kN}$, $C_{190\ kN}$ and $C_{200\ kN}$. The images produced by the nominal load corresponding to that class and those generated by loads that are very close to the nominal one belong to the same class. In a similar way, the class of images related to the plate in the absence of loads has been obtained (60 × 4 images). As a testing database, 60 × 4 images have been produced by subjecting a plate of the same characteristics with different symmetrical bi-axial loads supposed unknown. For our purposes, each 2D EC map is represented as a gray-scale image. Next two sections describe in detail the proposed approach to solve the problem under study.

4 Proposed method

4.1 EC maps as fuzzy images: some basic concepts

A 2D EC map with L gray levels can be considered as a 2D image, indicated by $\mathbf{I}$, constituted by $M \times N$ elements (i, j), with $i = 1, \ldots, M$ and $j = 1, \ldots, N$ (pixels of $\mathbf{I}$). Let us associate with each element, (i, j), its corresponding gray level, a_{ij}. On $\mathbf{I}$, a fuzzy membership function

$$m_I(a_{ij}): \mathbf{I} \rightarrow [0, 1] \tag{9}$$

can be chosen to formalize how much a_{ij} belongs, in a fuzzy sense, to I. In particular, if

$$m_{\mathbf{I}}(a_{ij}) = 1, \tag{10}$$

6 Hot rolled steel for open profiles: specific weight $\gamma = 78.5\ kN/m^3$; Young's modulus $E = 2,10,000$ MPa; shear modulus of elasticity $G = 80,769$ MPa.

7 The 2D image is suitably nuanced through the MatLab shading interp function.

a_{ij} totally belongs to **I**; if

$$m_{\mathbf{I}}(a_{ij}) = 0, \tag{11}$$

a_{ij} does not totally belong to **I**; finally, if $m_I(a_{ij}) \in (0, 1)$, a_{ij} partially belongs to **I**.

Let us consider $F(\mathbf{I})$ as the fuzzified image of **I** whose pixels represent the quantity $m_{\mathbf{I}}(a_{ij})$, $i = 1, \ldots, M$ and $j = 1, \ldots, N$.

4.2 Choice of the membership function

The approach presented here to make a suitable membership function exploits the intensification operator to reduce the fuzziness and, at the same time, to enhance the contrast of the image itself. So, if $F_e = F_d = 0.5$ are two suitable fuzzifiers, to control the amount of grayness ambiguity, the membership function could be defined as follows [14,15]:

$$m'_{\mathbf{I}}(a'_{ij}) = (1 + (\max(a'_{ij}) - a'_{ij})F_d^{-1})^{F_e}, \tag{12}$$

where a'_{ij} represents the gray levels of the generic image before the application of the pre-processing procedure (reduction of fuzziness and contrast enhancement). It is worth noting that in (12) $m'_{\mathbf{I}}(a'_{ij})$ goes to 1 if a'_{ij} goes to $\max(a_{ij})$ (maximum brightness condition). To achieve $m_I(a_{ij})$ (as required in Section 4.1), we exploit the intensifier operator to stretch the contrast among membership values [14,15]. That is,

$$\begin{cases} m_{\mathbf{I}}(a_{ij}) = 2(m'_{\mathbf{I}}(a'_{ij}))^2 & \text{if } 0 \le m'_{\mathbf{I}}(a'_{ij}) \le 0.5 \\ m_{\mathbf{I}}(a_{ij}) = 1 - 2(1 - m'_{\mathbf{I}}(a'_{ij}))^2 & \text{if } 0.5 \le m'_{\mathbf{I}}(a'_{ij}) \le 1 \\ i = 1, \ldots, M; \quad j = 1, \ldots, N. \end{cases} \tag{13}$$

From (13), by using the inverse function, we obtain the final values of each gray level as follows:

$$\begin{cases} a_{ij} = \max(a_{ij}) - F_d\{(m_{\mathbf{I}}(a_{ij}))^{1/F_e} - 1\} \\ i = 1, \ldots, M; \quad j = 1, \ldots, N. \end{cases}$$

4.3 Fuzziness quantification in a fuzzy image

Once a fuzzy image $F(\mathbf{I})$ is achieved, it is important to evaluate its fuzziness by means of "*ad-hoc*" index of fuzziness (IoF), denoting the degree of ambiguity present in $F(\mathbf{I})$ [14,15] to justify the applicability of the proposed procedure. Considering the distance between $m_{\mathbf{I}}(a_{ij})$ and the membership values of the nearest ordinary set $\widehat{m_{\mathbf{I}}(a_{ij})}$, $d(m_{\mathbf{I}}(a_{ij}), \widehat{m_{\mathbf{I}}(a_{ij})})$, IoF can be defined as follows[8]:

$$\text{IoF} = 2(M \times N)^{-0.5} d(m_{\mathbf{I}}(a_{ij}), \widehat{m_{\mathbf{I}}(a_{ij})}). \tag{14}$$

In this work, $d(m_{\mathbf{I}}(a_{ij}), \widehat{m_{\mathbf{I}}(a_{ij})})$ has been computed in terms of axiomatic fuzzy divergence (for details, see [14,15,20]), here indicated by AFD [23], because it gives a fuzzy measurement of the distance between $m_{\mathbf{I}}(a_{ij})$ and $\widehat{m_{\mathbf{I}}(a_{ij})}$ distinguishing if the differences between them are in low or high membership value.[9]

4.4 Fuzzy similarities and fuzzy images

Let us indicate by $F(\mathbf{I}_x)$ and $F(\mathbf{I}_y)$ two different $M \times N$ fuzzy images whose pixels are $m_{\mathbf{I}_x}(a_{ij})$ and $m_{\mathbf{I}_y}(b_{ij})$ with $i = 1, \ldots, M$ and $j = 1, \ldots, N$, respectively. In a fuzzy context, both $F(\mathbf{I}_x)$ and $F(\mathbf{I}_y)$ can be considered as two fuzzy sets whose membership functions are $m_{\mathbf{I}_x}(a_{ij})$ and $m_{\mathbf{I}_y}(b_{ij})$, respectively. Furthermore, U indicates the universe of discourse such that both $F(\mathbf{I}_x)$ and $F(\mathbf{I}_y)$ belong to U. To define an FS measure, we need to define a function

$$\text{FS}: F(\mathbf{I}_x) \times F(\mathbf{I}_y) \to [0, 1] \tag{15}$$

satisfying the following four properties.

1. Property of reflexivity, which establishes that each image is similar to itself with the maximum degree, must be verified:

$$\forall F(\mathbf{I}_x) \in U \Rightarrow \text{FS}(F(\mathbf{I}_x), F(\mathbf{I}_x)) = \max_{\forall F(\mathbf{I}_x), F(\mathbf{I}_y) \in U} \text{FS}(F(\mathbf{I})_x, F(\mathbf{I})_y) = 1. \tag{16}$$

2. FS must be symmetric. In other words, it should not depend on the order in which the fuzzy images are taken into account. That is,

$$\text{FS}(F(\mathbf{I}_x), F(\mathbf{I}_y)) = \text{FS}(F(\mathbf{I}_y), F(\mathbf{I}_x)). \tag{17}$$

3. In addition,

$$\forall F(\mathbf{I}_x) \in U \Rightarrow \text{FS}(F(\mathbf{I}_x), \overline{F(\mathbf{I}_x)}) = 0, \tag{18}$$

where $\overline{F(\mathbf{I}_x)}$ represents the complementary fuzzy image of $F(\mathbf{I}_x)$ such that its membership values are computed as $1 - m_{\mathbf{I}_x}(a_{ij})$.

4. Finally, $\forall F(\mathbf{I}_x), F(\mathbf{I}_y), F(\mathbf{I}_z) \in U$, if[10]

$$m_{\mathbf{I}_x}(a_{ij}) \le m_{\mathbf{I}_y}(b_{ij}) \le m_{\mathbf{I}_z}(c_{ij}) \tag{19}$$

---

8 $\widehat{m_{\mathbf{I}}(a_{ij})} = 0$, if $m_{\mathbf{I}}(a_{ij}) \le 0.5$. $\widehat{m_{\mathbf{I}}(a_{ij})} = 1$, otherwise.

9 It is possible, because $m_{\mathbf{I}}(a_{ij}) \in C^0[(0, 1)]$ (metric space). In addition, it is easy to prove that AFD, as in [20] formulated, satisfies the axioms of distances in metric spaces.

10 That is, $F(\mathbf{I}_x) \subset F(\mathbf{I}_y) \subset F(\mathbf{I}_z)$.

with a_{ij}, b_{ij} and c_{ij} the gray levels of $\mathbf{I}_x$, $\mathbf{I}_y$ and $\mathbf{I}_z$, respectively, then

$$\mathrm{FS}(F(\mathbf{I}_x), F(\mathbf{I}_y)) \geq \mathrm{FS}(F(\mathbf{I}_x), F(\mathbf{I}_z)) \tag{20}$$

and

$$\mathrm{FS}(F(\mathbf{I}_y), F(\mathbf{I}_z)) \geq \mathrm{FS}(F(\mathbf{I}_x), F(\mathbf{I}_z)). \tag{21}$$

4.5 Suitable formulations of fuzzy similarities

For our purposes, with respect to the four required properties specified in Section 4.4, we need to exploit FS formulations with low computational load particularly useful for real-time applications. With this goal in mind, excellent candidates are the Chaira FSs [14,15] that, properly adapted to the case under study, take the following form:

$$\mathrm{FS}_1(F(\mathbf{I}_x), F(\mathbf{I}_y)) = \frac{1}{M \times N} \times \sum_{i=1}^{M}\sum_{j=1}^{N}\left(\frac{\min(m_{\mathbf{I}_x}(a_{ij}), m_{\mathbf{I}_y}(b_{ij}))}{\max(m_{\mathbf{I}_x}(a_{ij}), m_{\mathbf{I}_y}(b_{ij}))}\right); \tag{22}$$

$$\mathrm{FS}_2(F(\mathbf{I}_x), F(\mathbf{I}_y)) = 1 - \frac{\sum_{i=1}^{M}\sum_{j=1}^{N}|m_{\mathbf{I}_x}(a_{ij}), m_{\mathbf{I}_y}(b_{ij})|}{\sum_{i=1}^{M}\sum_{j=1}^{N}(m_{\mathbf{I}_x}(a_{ij}) + m_{\mathbf{I}_y}(b_{ij}))}; \tag{23}$$

$$\mathrm{FS}_3(F(\mathbf{I}_x), F(\mathbf{I}_y)) = \sum_{i=1}^{M}\sum_{j=1}^{N}\frac{2\min(m_{\mathbf{I}_x}(a_{ij}), m_{\mathbf{I}_y}(b_{ij}))}{m_{\mathbf{I}_x}(a_{ij}) + m_{\mathbf{I}_y}(b_{ij})}; \tag{24}$$

$$\mathrm{FS}_4(F(\mathbf{I}_x), F(\mathbf{I}_y)) = \max(\min(m_{\mathbf{I}_x}(a_{ij}), m_{\mathbf{I}_y}(b_{ij}))). \tag{25}$$

Obviously, if

$$m_{\mathbf{I}_x}(a_{ij}) + m_{\mathbf{I}_y}(b_{ij}) = 0, \tag{26}$$

then

$$\mathrm{FS}(F(\mathbf{I}_x), F(\mathbf{I}_y)) = 1 \tag{27}$$

so that both (24) and (25) still have meaning. Finally, it is worth noting that

$$1 - \mathrm{FS}_1(F(\mathbf{I}_x), F(\mathbf{I}_y)), \tag{28}$$

$$1 - \mathrm{FS}_2(F(\mathbf{I}_x), F(\mathbf{I}_y)), \tag{29}$$

$$1 - \mathrm{FS}_3(F(\mathbf{I}_x), F(\mathbf{I}_y)) \tag{30}$$

and

$$1 - \mathrm{FS}_4(F(\mathbf{I}_x), F(\mathbf{I}_y)) \tag{31}$$

are measurements of distances among fuzzy images because satisfying all the properties for distances in $C^0([0,1])$ in which they are defined [14,15]. Then, by complementarity, all FS formulations considered here quantify how much two fuzzy images are similar to each other.

4.6 Construction of the $\tilde{N}$ classes starting from the $\tilde{N}$ external bi-axial load conditions

Let $\tilde{N}$ be the number of external bi-axial loads. If $k = 1, \ldots \tilde{N}$, for the avoidance of doubt, we indicate by $F(\mathbf{I_k})$ the representative 2D EC image of the kth class of loads considered similar to each other. In addition, $F(\mathbf{I_{un}})$ is a 2D EC image achieved with an unknown external bi-axial load, while $F(\mathbf{I}_{\text{No Load}})$ is the 2D EC image related to steel plates not subject to any external load. Having as a purpose the association of an unknown load with one of the $\tilde{N}$ known classes, $\forall\, k = 1, \ldots \tilde{N}$, we compute the following sets of scalar quantities:

$$A = \{\mathrm{FS}_1(F(\mathbf{I_{un}}), F(\mathbf{I_1})), \ldots, \mathrm{FS}_1(F(\mathbf{I_{un}}), F(\mathbf{I}_k)), \ldots, \mathrm{FS}_1(F(\mathbf{I_{un}}), F(\mathbf{I}_{\tilde{N}})), \mathrm{FS}_1(F(\mathbf{I_{un}}), F(\mathbf{I}_{\text{No Load}}))\} \tag{32}$$

$$B = \{\mathrm{FS}_2(F(\mathbf{I_{un}}), F(\mathbf{I_1})), \ldots, \mathrm{FS}_2(F(\mathbf{I_{un}}), F(\mathbf{I_k})), \ldots, \mathrm{FS}_2(F(\mathbf{I_{un}}), F(\mathbf{I_{\tilde{N}}})), \mathrm{FS}_2(F(\mathbf{I_{un}}), F(\mathbf{I}_{\text{No Load}}))\} \tag{33}$$

$$C = \{\mathrm{FS}_3(F(\mathbf{I_{un}}), F(\mathbf{I_1})), \ldots, \mathrm{FS}_3(F(\mathbf{I_{un}}), F(\mathbf{I_k})), \ldots, \mathrm{FS}_3(F(\mathbf{I_{un}}), F(\mathbf{I_{\tilde{N}}})), \mathrm{FS}_3(F(\mathbf{I_{un}}), F(\mathbf{I}_{\text{No Load}}))\} \tag{34}$$

$$D = \{\mathrm{FS}_4(F(\mathbf{I_{un}}), F(\mathbf{I_1})), \ldots, \mathrm{FS}_4(F(\mathbf{I_{un}}), F(\mathbf{I_k})), \ldots, \mathrm{FS}_4(F(\mathbf{I_{un}}), F(\mathbf{I_{\tilde{N}}})), \mathrm{FS}_4(F(\mathbf{I_{un}}), F(\mathbf{I}_{\text{No Load}}))\}. \tag{35}$$

Then,

$$\mathrm{FS}_\chi(F(\mathbf{I_{un}}), F(\mathbf{I_{\bar{k}}})), \quad \chi = 1, 2, 3, 4 \tag{36}$$

and

$$\bar{\mathbf{k}} \in \{1, \ldots, \tilde{N} + 1\}, \tag{37}$$

which gives us the quantity

$$\sup\{\sup\{A\}, \sup\{B\}, \sup\{C\}, \sup\{D\}\} \tag{38}$$

that determines the association of the unknown load with the class $\bar{\mathbf{k}}$. The following section explains how $F(\mathbf{I_k})$, $\forall\, \mathbf{k} = 1, \ldots, \tilde{N} + 1$ are made.

5 Representative 2D EC image of each class of loads: a fuzzy image fusion approach

In order to get, $F(\mathbf{I_k})$, $\forall\, \mathbf{k} = 1, \ldots, \tilde{N} + 1$, we propose a simple fuzzy pixel level data fusion technique by exploiting FS_χ values ($\chi = 1, 2, 3, 4$). First, we indicate

by $F(\mathbf{I}_{\mathbf{k}}^{s})$ and $F(\mathbf{I}_{\mathbf{k}}^{z})$ with $s, z \in P = \{1, \ldots, 60\}$ two generic images belonging to the generic class $\mathbf{k}$. With these premises, the following six steps describe the proposed procedure.

1. We initially subdivide $F(\mathbf{I}_{\mathbf{k}}^{s})$ and $F(\mathbf{I}_{\mathbf{k}}^{z})$, $\forall\ s,\ z \in P$, into T not overlapped subimages (10 × 10 pixels). Let them be $F(\mathbf{I}_{\mathbf{k}}^{s})_{t_1}$ and $F(\mathbf{I}_{\mathbf{k}}^{z})_{t_2}$, $t_1, t_2 \in H = \{1, \ldots, T\}$.
2. Then, we compute

$$\mathrm{FS}_{\chi}(F(\mathbf{I}_{\mathbf{k}}^{s})_1, F(\mathbf{I}_{\mathbf{k}}^{z})_1), \quad \chi = 1, 2, 3, 4 \tag{39}$$

   and $s, z \in P$.
3. Let

$$(F(\mathbf{I}_{\mathbf{k}}{}^{\bar{s}})_1, F(\mathbf{I}_{\mathbf{k}}{}^{\bar{z}})_1), \quad \bar{s}, \bar{z} \in P, \tag{40}$$

   be the pair of subimages providing

$$\max\{\mathrm{FS}_{\chi}(F(\mathbf{I}_{\mathbf{k}}{}^{\bar{s}})_1, F(\mathbf{I}_{\mathbf{k}}{}^{\bar{z}})_1)\}. \tag{41}$$

4. Indicating by $F(\mathbf{I}_{\mathbf{k}})_1$ the portion of $F(\mathbf{I}_{\mathbf{k}})$ corresponding (in terms of pixel positions, (i, j)) to the subimages $F(\mathbf{I}_{\mathbf{k}}^{s})_1$ and $F(\mathbf{I}_{\mathbf{k}}^{z})_1$, we pose:

$$[F(\mathbf{I}_{\mathbf{k}})_1]_{(i,j)} = \left(1 + e^{-\frac{[F(\mathbf{I}_{\mathbf{k}}^{s})_1]_{(i,j)} + [F(\mathbf{I}_{\mathbf{k}}^{z})_1]_{(i,j)}}{2}}\right)^{-1} \tag{42}$$

   in order that each pixel belonging to $F(\mathbf{I}_{\mathbf{k}})_1$ is achieved by the sigmoidal smoothing approach on the arithmetic average of the corresponding pixels of both $F(\mathbf{I}_{\mathbf{k}}^{s})_1$ and $F(\mathbf{I}_{\mathbf{k}}^{z})_1$.
5. Repeat steps (1)–(4), $\forall\ t_1, t_2 \in H$ obtaining the fuzzy image $F(\mathbf{I}_{\mathbf{k}})$ related to the $\mathbf{k}$th class of external bi-axial loads.
6. To achieve all of the fuzzy images related to all classes, it is sufficient to repeat steps (1)–(5), $\forall\ \mathbf{k} = 1, \ldots, \tilde{N} + 1$.

6 A brief overview of the techniques used to compare the results

To compare the quality of the results obtained by the proposed procedure, the classification has also been carried out through fuzzy inference systems (FISs; Mamdani and Sugeno types), Fuzzy *K*-means clustering technique and self-organizing map (SOM).

6.1 FISs: Mamdani and Sugeno approaches

An FIS realizes an input/output (I/O) mapping by means of inference based on IF – THEN linguistic rules in which the I/O variables are linguistic, because they assume linguistic values mathematically expressed by fuzzy sets [24–26]. In order to compute the output starting from the inputs, Mamdani's approach needs the following six steps: (1) determination of the bank of fuzzy rules; (2) fuzzification of the inputs by means of fuzzy membership functions; (3) combination of the fuzzified inputs according to the bank of fuzzy rules to establish a rule strength (fuzzy operations); (4) finding the consequence of the rule by combining the rule strength and the output membership function (implication); (5) combination of the consequences for getting the output distribution (aggregation); and (6) defuzzification of the output distribution. Unlike Mamdani's approach, Sugeno's method considers polynomial functions as output membership functions so that the final output is the weighted average of the all rules output. For our purposes, by means of MatLab® Fuzzy Toolbox it has been made a Mamdani FIS, whose bank of fuzzy rules is constituted by 25 fuzzy rules with four multiple antecedents,

$$\mathrm{FS}_{\chi}(F(\mathbf{I}_{\mathbf{k}}), F(\mathbf{I}_{\mathbf{k}}{}^{s})) \tag{43}$$

with

$$\chi = 1, \ldots, 4, \quad s \in P \tag{44}$$

and

$$\forall\ \mathbf{k} = 1, \ldots, \tilde{N} + 1, \tag{45}$$

while the outputs are the six classes as mentioned above. In addition, an automatic Sugeno FIS has been extracted using the same Toolbox with 28 fuzzy rules with the same I/O pairs.

6.2 Fuzzy *k*-means approach and SOM maps

Here, a variation in the well-known unsupervised learning algorithm [24,27] for clustering problems has been implemented by the MatLab® Fuzzy Clustering Toolbox. Fixing *a priori* six clusters (the six classes considered as output), they will be centered far away from each other. Then, each point of a given data set (FS_{χ} as described above) has been associated with the nearest cluster. The new positions of the cluster centers have been computed by minimization of a squared error objective function depending on the distance measure between data points and cluster centers. SOMs are particular artificial neural networks trained by an unsupervised learning producing a 2D discretized map of the input space [28,29]. In particular, the training

operation builds the 2D map exploiting input data (by means of a competitive process), while the mapping procedure classifies automatically new input data. For our purposes, in this work an SOM with FS_χ has been taken into account and implemented by the MatLab® SOM Toolbox.

7 Some relevant results

The procedure described in Sections 4 and 5 has been implemented on Intel Core 2 CPU 1.47 GHz and MatLab® R2017a. Preliminarily, for each class of external bi-axial loads, the ranges of IoFs have been computed. Their high values highlight high fuzziness in the images belonging in each class as well as the values of IoF related to each $F(\mathbf{I_k})$ (Table 3). These high values justify the application of the proposed fuzzy procedure. As shown in Table 4, the proposed technique correctly classifies the cases under examination with a percentage of over 99.4% but variable according to the type of image (real and imaginary parts, module and phase of pick-up voltage). These percentages slightly increase when FS_3 is considered with the advantage of reducing the related CPU-time. So, for real-time application, FS_3 appears as the best candidate among the FS_χ proposed in this work. In Figure 4, a classification example is shown by the proposed procedure from which it is clear that the 2D EC image belongs to $C_{190\ kN}$ (blue bars represent the maximum admissible value of FSs equal to unity; red bars represent the computed FS values). Finally, the classification obtained by all FS_χ can be considered as a good performance comparable to the performances obtained with the other techniques exploited here but characterized by a higher computational complexity as shown by the increase in CPU-time values.

Table 3: Ranges of IoF related to the images belonging to each class and to each $F(\mathbf{I_k})$ as well

Class	Range of IoF	IoF of $F(\mathbf{I_k})$	Class	Range of IoF	IoF of $F(\mathbf{I_k})$
$C_{160\ kN}$	0.92–0.97	0.95	$C_{160\ kN}$	0.79–0.83	0.80
$C_{180\ kN}$	0.88–0.91	0.90	$C_{190\ kN}$	0.80–0.86	0.84
$C_{200\ kN}$	0.79–0.85	0.83	Without loads	0.83–0.91	0.89

8 Conclusions and perspectives

In this article, a novel approach based on FS computations for the assessment of the integrity of steel plates under an external bi-axial load is proposed. Through EC testing, 2D electrical maps related to the 2D distribution of deformations on a plate have been experimentally achieved and grouped into different classes satisfying the principle according to which similar external bi-axial loads produce similar deformation distributions. Fuzzifying properly all the obtained 2D maps and evaluating their fuzziness using a suitable index, 2D maps representative of each class are obtained exploiting a new approach based on the fuzzy image fusion. Finally, four different FS formulations have been presented and used to determine the association of an unknown load (and, therefore, the distribution of deformations generated by it) with a specific class of external loads. By the proposed approach, on one hand, the determination of the deformations in a steel plate is translated in terms of a suitable classification problem and, on the other hand, the theoretical computation of mechanical deformations is translated into an experimental

Table 4: Performance of classification compared to other soft computing techniques

Technique	CPU time (s)	Pick-up voltage (real part) (%)	Pick-up voltage (imaginary part) (%)	Pick-up voltage (module) (%)	Pick-up voltage (phase) (%)
FS_1	0.45	99.6	99.5	99.6	99.6
FS_2	0.43	99.4	99.4	99.4	99.2
FS_3	0.34	99.8	99.9	99.7	99.8
FS_4	0.25	99.6	99.5	99.6	99.6
FIS (Mamdani)	0.45	99.1	99.4	99.4	99.3
FIS (Sugeno)	1.05	99.9	99.9	99.8	99.9
FKM	1.23	99.7	99.5	99.7	99.6
SOM	0.99	99.8	99.6	99.8	99.7

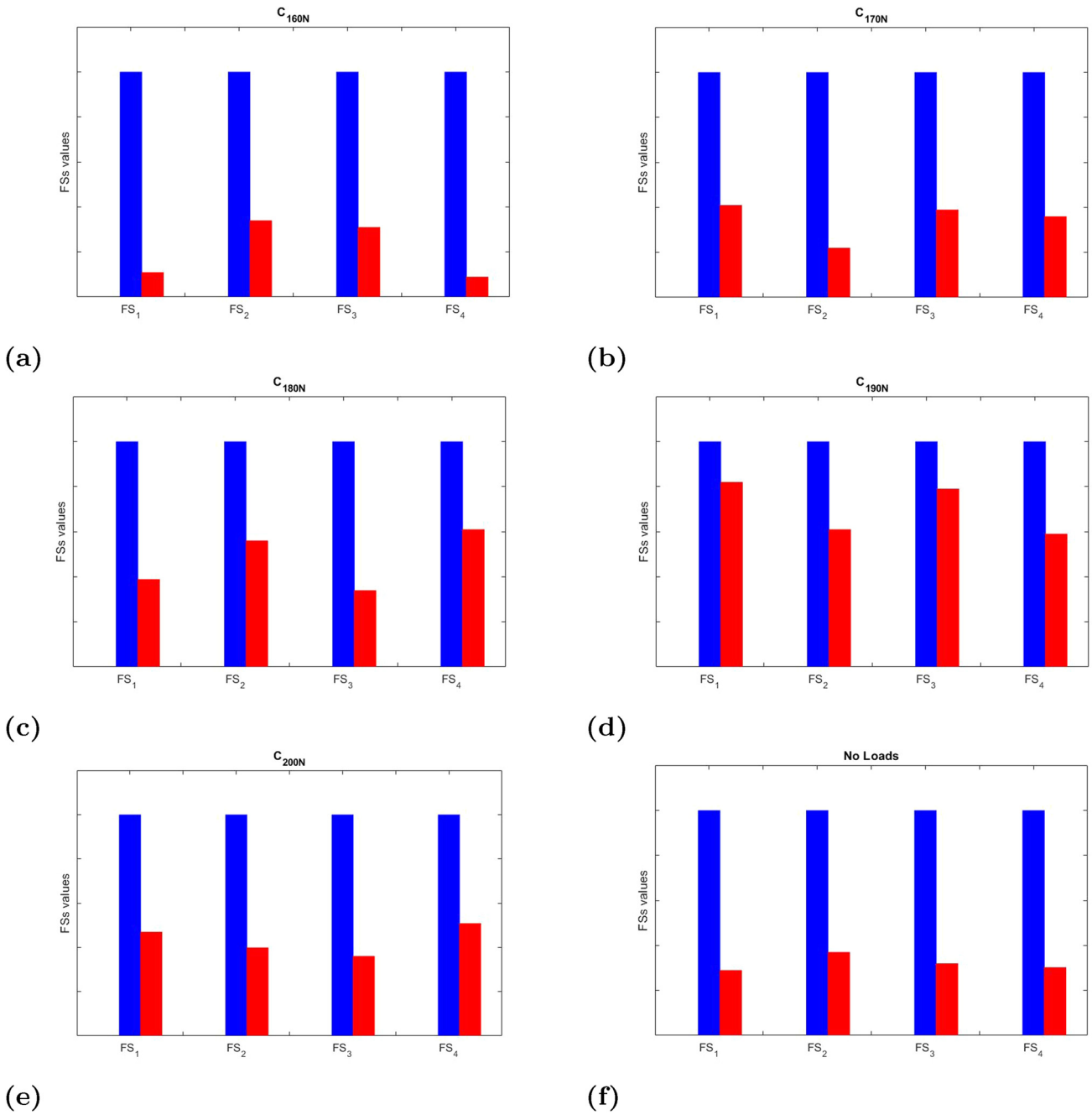

Figure 4: An example of classification related to an unknown 2D EC image. (a–f) show the FS values obtained with the images representing $C_{160\ kN}$, $C_{170\ kN}$, $C_{180\ kN}$, $C_{190\ kN}$, $C_{200\ kN}$, no load, respectively. It is clear that the unknown 2D EC image belongs to $C_{190\ kN}$.

campaign of EC measurements with portable instrumentation (useful for *in situ* real-time applications). The obtained results can be considered encouraging because they have put in evidence performances of classification comparable with other well-established soft computing procedures characterized by a higher computational complexity. However, a better formalization of the proposed procedure, assisted by a more careful selection of FS formulations, will surely improve the performance of the proposed approach. In addition, the use of step function voltage to excite the probe is desirable because a single-step function contains a set of frequencies and, since the penetration depth depends on the frequency, they acquired simultaneously information from a range of depth. Last but not least, it seems useful to take into account vagueness and/or uncertainty phenomena due to inhomogeneity of the morphological structure of the material, which inevitably affects the distributions of

magnetic permeability and electrical conductivity of the specimen.

References

[1] Landolfo R, Mazzolani F, Dubina D, da Silva LS, D'Aniello M. Design of steel structures for buildings in seismic areas: Eurocode 8: design of structures for earthquake resistance. Part 1-1 – general rules, seismic actions and rules for buildings. Wilhelm Ernst & Sohn Verlag für Architektur und technische Wissenschaften GmbH & Co. KG, Berlin: Wiley Online Library; 2017.

[2] Burrascano P, Callegari S, Montisci A, Ricci M, Versaci M. Ultrasonic nondestructive evaluation systems: industrial application issues. Switzerland: Springer International Publishing; 2015.

[3] Pavo J, Gasparics A, Sebestyen I, Vertesy G, Darczi CS, Miya K. Eddy current testing with fluxset probe, applied electromagnetics and mechanincs. Tokyo: JSAEM; 1996.

[4] Repelianto AS, Kasai N. The improvement of flaw detection by the configuration of uniform eddy current probe. Sensors. 2019;19:1–13.

[5] Adewale ID, Tian GY. Decoupling the influence of permeability and conductivity in pulsed eddy-current measurements. IEEE Trans Magnet. 2012;49(3):1119–27.

[6] Chao CY. Bifurcation and stability of homogeneous of an elastic body under load tractions with $Z2$ symmetry. J Elast. 1991;25:117–36.

[7] Ericksen JL. Equilibrium of bar. J Elasicity. 1975;25:191–201.

[8] Carter CB, Norton MG. Solid-state phase transformations and reactions, ceramic materials. New York, NY: Springer; 2006.

[9] Silva AR, Dias LES. An interface element for numerical analysis of flat plate/shell elements with eeformable connection. Lat Am J Solids Struct. 2019;15:1–16.

[10] Duggal SK. Limit state design of steel structures. McGraw Hill Education Pvt Ltd; 2014.

[11] Sophian A, Tian G, Fan M. Pulsed eddy current non-destructive testing and evaluation: a review. Chin J Mech Eng. 2017;30:500–14. doi: 10.1007/s10033-017-0122-4

[12] Versaci M, Angiulli G, Di Barba P, Morabito FC. 2D Eddy Currents Imaging & Fuzzy Similarities for Assessing the Integrity of Steel Plates, In: Proceedings of 19th International Symposium on Electromagnetic Fields in Mechatronics, Electrical and Electronic Engineering (29–31 August 2019, Nancy, France), Nancy, 2019.

[13] Bowler N. Eddy-current nondestructive evaluation. New York, NY: Springer; 2019.

[14] Chaira T, Ray AK. Fuzzy image processing and application with MatLab. CRC Press, Taylor & Francis Group; 2012.

[15] Chaira T. Medical image processing – advanced fuzzy set theoretic techniques. Abingdon, OX14 4RN: CRC Press, Taylor & Francis Group; 2015.

[16] Pal A, Mondal B, Bhattacharyya N, Raha S. Similarity in fuzzy systems. J Uncertain Anal Appl. 2014;2(18):1–28.

[17] Baccour L, Alimi AM, Joh RI. Some notes on fuzzy similarity measures and application to classification of shapes, recognition of arabic sentences and mosaic. IAENG Int J Comput Sci. 2014;41(2):1–10.

[18] Versaci M. Fuzzy approach and eddy currents NDT/NDE devices in industrial applications. Electron Lett. 2016;52(11):943–5.

[19] Angiulli G, Versaci M, Neuro-Fuzzy A. Network for the design of circular and triangular equilateral microstrip antennas. Int J Infrared Millim Waves. 2002;23(10):1513–20.

[20] Morabito FC, Versaci M, Pautasso G, Tichmann C. Fuzzy-neural approaches to the prediction of disruptions in ASDEX upgrade. Nucl Fusion. 2001;41(11):1715–23.

[21] Ball JM, Janes RD. Fine phase mixture as minimizers of energy. Arch Ration Mech Anal. 1987;100:13–52.

[22] Versaci M, Morabito FC. Fuzzy time series approach for disruption prediction in tokamak reactors. IEEE Trans Magnet. 2003;39:1503–6, doi: 10.1109/TMAG.2003.810365

[23] Versaci M, La Foresta F, Morabito FC, Angiulli G. A fuzzy divergence for solving electrostatic identification problems for NDT applications. Int J Appl Electromagnet Mech. 2018;57(2):133–46.

[24] Bede B. Mathematics of Fuzzy Sets and Fuzzy Logic. Springer, Berlin, Heidelberg: Springer-Verlag Berlin Heidelberg; 2013.

[25] Morabito FC. Independent component analysis and feature extraction techniques for NDT data. Mater Eval. 2000;58(1):85–92.

[26] Morabito FC, Versaci M, Fuzzy A. Neural approach to localizing holes in conducting plates. IEEE Trans Magnet. 2001;37(5I):3534–7.

[27] El-Harby AA, Algrafy E. Efficient neuro-fuzzy inference systems (ANFIS) and neural network systems for different beams collisions with light nuclei. Asian J Sci Res. 2019;12(1):71–78.

[28] Aggarwal CC. Neural Networks and Deep Learning. Switzerland: Springer; 2018.

[29] Mishra S, Panda M. Medical image retrieval using self-organising map on texture features. Fut Comput Inform J. 2018;3(2):359–70.